ACSNANO
www.acsnano.org
ARTICLE

# Biodegradable Photonic Melanoidin for Theranostic Applications

Min-Young Lee,[†,⊥,§] Changho Lee,[‡,§] Ho Sang Jung,[†,§] Mansik Jeon,[‡,∥] Ki Su Kim,[#] Seok Hyun Yun,[#] Chulhong Kim,[*,‡] and Sei Kwang Hahn[*,†,‡]

[†]Department of Materials Science and Engineering and [‡]Department of Creative IT Engineering, Pohang University of Science and Technology (POSTECH), 77 Cheongam-ro, Nam-gu, Pohang, Gyeongbuk 790-784, Korea

[⊥]Medical Device Research Center, Samsung Biomedical Research Institute, Samsung Advanced Institute of Technology (SAIT), Samsung Electronics Company Ltd., Seoul 135-710, Korea

[#]Wellman Center for Photomedicine, Harvard Medical School and Massachusetts General Hospital, 65 Landsdowne Street UP-5, Cambridge, Massachusetts 02139, United States

Supporting Information

**ABSTRACT:** **Light-absorbing nanoparticles for localized heat generation in tissues have various biomedical applications in diagnostic imaging, surgery, and therapies. Although numerous plasmonic and carbon-based nanoparticles with strong optical absorption have been developed, their clearance, potential cytotoxicity, and long-term safety issues remain unresolved. Here, we show that "generally regarded as safe (GRAS)" melanoidins prepared from glucose and amino acid offer a high light-to-heat conversion efficiency, biocompatibility, biodegradability, nonmutagenicity, and efficient renal clearance, as well as a low cost for synthesis. We exhibit a wide range of biomedical photonic applications of melanoidins, including *in vivo* photoacoustic mapping of sentinel lymph nodes, photoacoustic tracking of gastrointestinal tracts, photothermal cancer therapy, and photothermal lipolysis. The biodegradation rate and renal clearance of melanoidins are controllable by design. Our results confirm the feasibility of biodegradable melanoidins for various photonic applications to theranostic nanomedicines.**

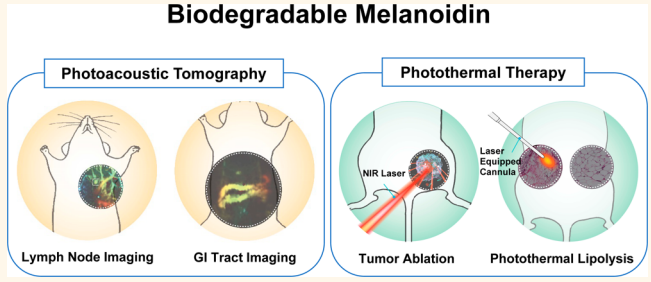


**KEYWORDS:** *melanoidin, biodegradable, photoacoustic, photothermal, theranostics*

The heat generation of light absorbing materials by nonionizing optical excitation is brought by light-triggered nonradiative energy decay. When an optically active substance heats up and expands by short-pulsed light irradiation, the released energy can be converted to acoustic waves, a signal source for photoacoustic tomography (PAT).[1−3] PAT has a unique feature of high ultrasonic resolution, showing strong light absorption contrast even in deep tissues. When a continuous-wave laser is used as the light source, the generated heat can be used for photothermal therapy (PTT) such as hyperthermia in cancer treatment.[4] Since intrinsic chromophores in biological tissues typically lack of optical absorption except hemoglobin and melanin,[2,3] there are strong medical demands to develop a clinically available and optically active contrast agent with a high light-to-heat conversion efficiency for both PAT and PTT.

A variety of inorganic nanomaterials (*e.g.*, Au-, Ag-, and Cu-based metal nanoparticles)[4−7] and carbon-based nanomaterials (*e.g.*, graphene and carbon nanotubes)[8] have been widely investigated as contrast agents for PAT and/or PTT. Recently, light-absorbing organic nanomaterials have been also reported as optically active agents for PAT and/or PTT, including porphyrin−lipid conjugates,[2] polypyrrole nanoparticles,[9] carbon nanoparticles produced by honey pyrolysis,[10] and semiconducting polymer nanoparticles.[11] Nevertheless, biocompatibility, biodegradability, renal clearance, and high heat conversion efficiency of these materials are still unmet needs for their clinical applications. In addition, carbon dots, synthesized by the pyrolysis of organic precursors, have been intensively investigated as an imaging probe. This pyrolysis process involves severe chemical and physical phase changes that can produce unexpected cytotoxic and mutagenic compounds.[12−14] For example, the treatment of glucose with heat or at nonphysiological pH results in the degradation to 5-hydroxymethylfurfural (HMF), 4-methylimidazole, formaldehyde, acetaldehyde, 2-furaldehyde, methylglyoxal, glyoxal, and

Received: September 21, 2015
Accepted: December 1, 2015
Published: December 1, 2015




DOI: 10.1021/acsnano.5b05931
*ACS Nano* 2016, 10, 822−831

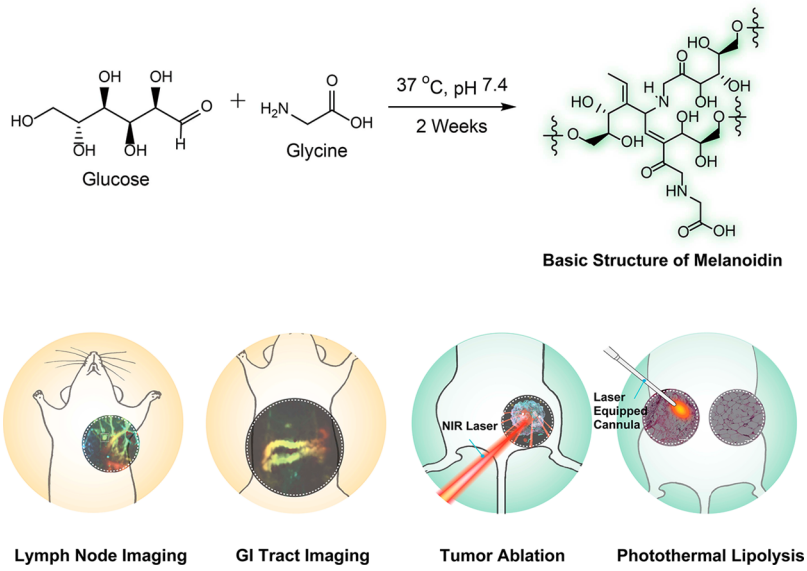


**Figure 1. Schematic representation and application of GG−melanoidin. Basic chemical structure of GG−melanoidin prepared by the Maillard reaction of glucose and glycine, and schematic illustration for various biomedical photonic applications of GG−melanoidin.**

some unidentified biologically active compounds.[15−18] Despite wide investigation of light absorbing materials for theranostic applications, there is no clinically available product until now due to the limited clearance and long-term safety issues.[19−21]

Here, we report a biocompatible, biodegradable, excretable by urinary system, and optically active synthetic polymer of melanoidin as a diagnostic contrast agent for PAT and as a therapeutic laser ablation transducer for PTT. Melanoidin is present in various foods such as coffee, dried fruit, bean paste, and soy sauce.[22−24] As a biomimetic approach, melanoidin could be synthesized by nonenzymatic Maillard reaction of glucose (G) and glycine (G) at body temperature and biological pH, avoiding the formation of cytotoxic and mutagenic compounds. To enhance the photothermal effect, we prepared GG−melanoidin/$Fe^{3+}$ complex by chelating Fe ions *via* the nitrogen in its structure.[22] GG−melanoidin and its complex were applied as theranostic nanomedicines to PAT for lymph node imaging and gastrointestinal (GI) tract imaging, and PTT for photothermal tumor ablation and lipolysis.

## RESULTS AND DISCUSSION

**Synthesis and Characterization of GG−Melanoidin.** Figure 1 shows the basic chemical structure of melanoidin,[25,26] which is very diverse depending on synthetic conditions such as temperature, pH, and reactant materials. A well-defined GG−melanoidin could be synthesized by the controlled Maillard reaction of glucose and glycine at body temperature and biological pH. Reducing glucose reacts with glycine to form a Schiff base adduct, which is then stabilized by Amadori rearrangement and polymerized. The synthesized GG−melanoidin contained hydroxyl and carboxyl groups that made it highly soluble and stable in water and serum without any stabilizer. At 37 °C and pH 7.4, the color of the glucose and glycine mixture changed to dark brown over time, whereas the color of a glucose solution did not change under the same condition. The size of GG−melanoidin could be controlled by changing the reaction time. Gel permeation chromatography (GPC) using various proteins as controls revealed that the molecular weight (MW) of melanoidin increased to 5.6 ± 0.3 kDa after reaction for 4 days, to 7.7 ± 0.5 kDa after 1 week, and to 10.3 ± 0.8 kDa after 2 weeks (Figure S1). For comparison, we prepared glucose carbon dots (GCDs) by the hydrothermal treatment (caramelization) of glucose at high temperature as previously reported elsewhere.[10,14,18]

The GG−melanoidin and GCD were compared by energy-dispersive X-ray spectroscopy (EDX), Fourier transform infrared spectroscopy (FT-IR), and $^1$H nuclear magnetic resonance (NMR). EDX spectra indicated that the GG−melanoidin contained 69.00 atomic (atom) % C, 11.05 atom % N, and 19.95 atom % O, and that GCD contained 71.63 atom % C and 28.37 atom % O (Figure 2a). According to the ratio of N to C in the GG−melanoidin, glucose and glycine appeared to be polymerized nearly at a ratio of 1. FT-IR spectra showed slight broadening and shift upon polymerization in peaks of both GG−melanoidin and GCD (Figure 2b). The GG−melanoidin spectrum showed no evidence of specific peaks of cytotoxic and mutagenic HMF at 1600−1610, 1510−1515, and 1390−1405 $cm^{-1}$. In contrast, the FT-IR spectrum of GCD showed new peaks in the 1390−1710 $cm^{-1}$ range, reflecting those of HMF.[18] On $^1$H NMR spectra, GG−melanoidin did not show the HMF peaks, whereas GCD did at $\delta$ = 6.6−6.7 ppm, $\delta$ = 7.4−7.5 ppm, and $\delta$ = 9.4−9.5 ppm (Figure S2).

**Preparation and Characterization of GG−Melanoidin/$Fe^{3+}$ Complex.** To increase the size of GG−melanoidin for more effective photothermal applications, we prepared GG−melanoidin/$Fe^{3+}$ complex (MW of GG−melanoidin = 10 kDa) by chelating Fe ions *via* the nitrogen in its structure.[22] The complex had a particle size of *ca.* 10 nm as shown in a TEM image (Figure 2c), and an elementary composition of C (68.23 atom %), N (12.14 atom %), O (16.02 atom %), and Fe (3.62 atom %) as shown in EDX spectrum (Figure 2d). *In vitro* release tests of Fe ions from GG−melanoidin/$Fe^{3+}$ complex for 24 h showed that only 0.86 ± 0.76% and 8.05 ± 2.1% of Fe ions were released in PBS and FBS solutions, respectively, maintaining the stable complex in the physiological condition (Figure S3).

**Photoacoustic Characterization of GG−Melanoidin.** The GG−melanoidin had a broad light absorption range at wavelengths from ultraviolet to near-infrared (NIR), and its absorption and photoacoustic signal increased with its MW at a



DOI: 10.1021/acsnano.5b05931
*ACS Nano* 2016, 10, 822−831

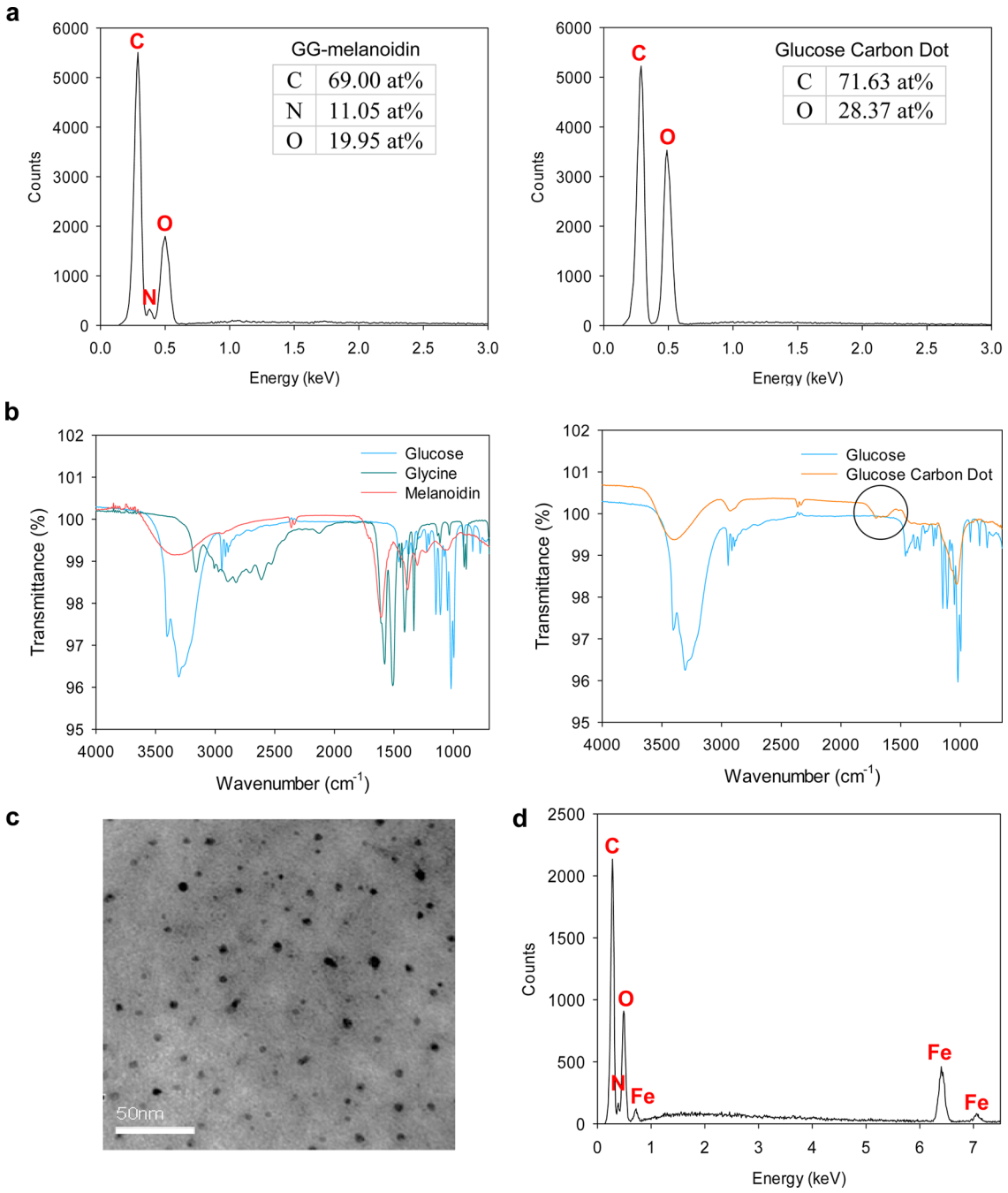


**Figure 2. Characterization of synthesized GG−melanoidin. (a) EDX spectra of (left) GG−melanoidin and (right) glucose carbon dot (GCD) prepared by hydrothermal treatment of glucose. (b) FT-IR spectra of (left) GG−melanoidin and (right) GCD. Circle indicates 5-hydroxymethyl furfural in GCD. (c) TEM image and (d) EDX spectrum of GG−melanoidin/$Fe^{3+}$ complex.**

given concentration (Figures 3a and S4). These absorption spectra are similar to that of graphene, carbon nanotubes, and several conducting polymers due to the conjugated systems of connected $\pi^*$ orbitals with delocalized $\pi$ electrons. The optical absorption of GG−melanoidin was affected by the amount of C═C and C═N bonds in the molecule, and the optical absorption peak shifted toward relatively long wavelengths with increasing MW. The extinction coefficient of GG−melanoidin with a MW of 5, 7, and 10 kDa was 0.18 ± 0.01, 0.37 ± 0.02, and 0.67 ± 0.04 mL/(mg/cm) at 680 nm, respectively. Furthermore, GG−melanoidin/$Fe^{3+}$ complex had significantly increased NIR absorption by a factor of 2.0 at $\lambda$ = 680 nm and 5.3 at $\lambda$ = 800 nm, compared to free GG−melanoidin (Figure S5). The optical absorption of GG−melanoidin increased with increasing concentration (Figure S6a). The PA signals decreased with increasing wavelength, but still could be detected at up to 900 nm. The PA signals *versus* various concentrations at an excitation wavelength of 680 nm showed a linear relationship (Figure S6b).

To examine the capability of GG−melanoidin and GG−melanoidin/$Fe^{3+}$ complex as contrast agents, the PA signals were directly compared at 680 nm with those of gold nanorod (AuNR) and FDA-approved methylene blue (MB) being widely used as a contrast agent for PAT (Figure S7).[4,11] At the same mass concentration, the normalized PA signals of GG−melanoidin (2.5 ± 0.1) and GG−melanoidin/$Fe^{3+}$ complex



DOI: 10.1021/acsnano.5b05931
*ACS Nano* 2016, 10, 822−831

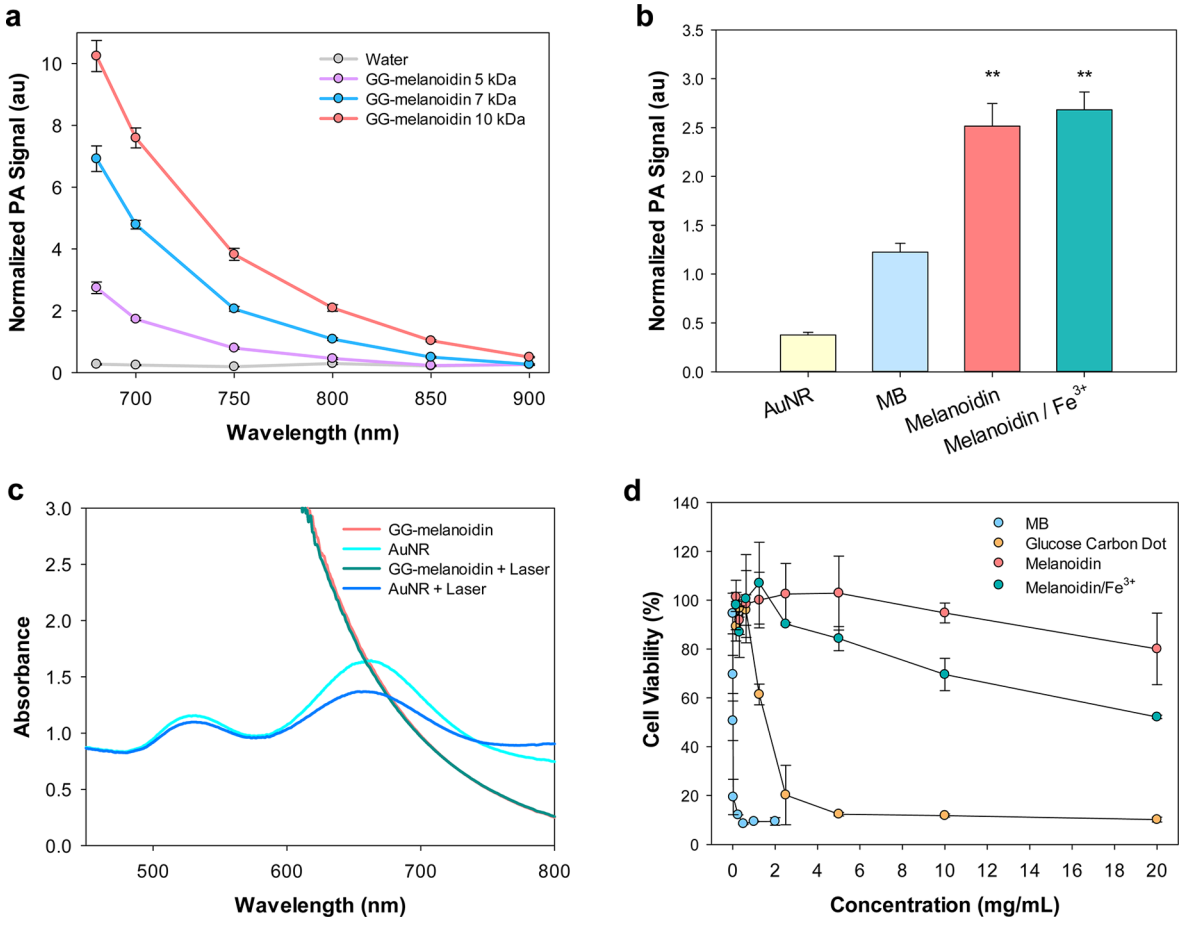


**Figure 3. Photoacoustic characteristics and biocompatibility of GG−melanoidin. (a) Photoacoustic spectra of GG−melanoidin with increasing molecular weight. (b) Photoacoustic signals at 680 nm of GG−melanoidin and GG−melanoidin/$Fe^{3+}$ complex in comparison with those of gold nanorod (AuNR) and methylene blue (MB) at the same optical density (**$P < 0.01$ for GG−melanoidin and GG−melanoidin/$Fe^{3+}$ complex *versus* AuNR and MB). (c) Optical absorbance measurement before and after 660 nm continuous laser irradiation for 10 min. (d) Cytotoxicity of GG−melanoidin and GG−melanoidin/$Fe^{3+}$ complex in comparison with MB and glucose carbon dot in hepatocytes of FL83B cells.**

(3.9 ± 0.2) were comparable to those of AuNR (3.0 ± 0.1) and MB (4.9 ± 0.2). However, at the same optical density, the PA signals of melanoidin (2.5 ± 0.2) and melanoidin/$Fe^{3+}$ complex (2.7 ± 0.2) were much higher than those of AuNR (0.4 ± 0.03) and MB (1.2 ± 0.1), respectively (Figure 3b). The possible reasons for the strong heat conversion efficiency of GG−melanoidin and GG−melanoidin/$Fe^{3+}$ complex at the same optical density include dominant nonradiative energy decay (*i.e.*, low fluorescence quantum yield), high heat conductance, high heat capacity, and negligible optical scattering in contrast to plasmonic gold nanomaterials.[3,11] Moreover, GG−melanoidin showed significantly higher optical stability than AuNR (Figure 3c). After 660 nm laser irradiation for 10 min, the optical absorption of GG−melanoidin changed from 1.65 to 1.62, whereas that of AuNR changed from 1.64 to 1.37.

***In Vitro* Cytotoxicity Test.** The biocompatibility of contrast agents is one of the most important issues for further clinical applications. The cytocompatibility of GG−melanoidin and GG−melanoidin/$Fe^{3+}$ complex was assessed in hepatocytes of FL83B cells, and compared with those of MB and GCD (Figure 3d). The viability of FL83B cells after incubation with GG−melanoidin was *ca.* 80% at the highest concentration of 20 mg/mL, which was significantly higher than that with GCD prepared by the hydrothermal treatment. GCD showed cell annihilation from the concentration of 2.5 mg/mL. The GG−melanoidin/$Fe^{3+}$ complex showed a cytotoxicity higher than that of GG−melanoidin, but lower than that of GCD. MB showed a very high cytotoxicity at a low concentration and killed all cells at concentrations above 0.025 mg/mL. At this concentration, the optical density of MB was only one-tenth of that of melanoidin at a concentration of 20 mg/mL. These results revealed the possibility of GG−melanoidin as a promising biocompatible theranostic agent.

**Photoacoustic Imaging of Sentinel Lymph Nodes.** First, we carried out PA imaging of sentinel lymph nodes (SLNs) using a reflection-mode PA imaging system with an optical wavelength of 680 nm (Figure S8). Noninvasive SLN mapping is clinically important for accurate staging of cancer patients.[2] The depth-encoded PA maximum amplitude projection (MAP) images and amplitude based PA images clearly showed the location of SLNs filled with melanoidin (Figures 4a and S9). Figure 4b shows the depth-sensitive cross-sectional PA images of Figure 4a, indicating the vertical location of the SLN in an axillary region (*i.e.*, 3 mm from the skin surface). Before injection of GG−melanoidin, PA MAP could visualize vasculatures below the skin, but not the SLNs. After intradermal injection of GG−melanoidin, the PA signal amplitude increased by 457.3 ± 260.6% at 83 min and then


DOI: 10.1021/acsnano.5b05931
*ACS Nano* 2016, 10, 822−831

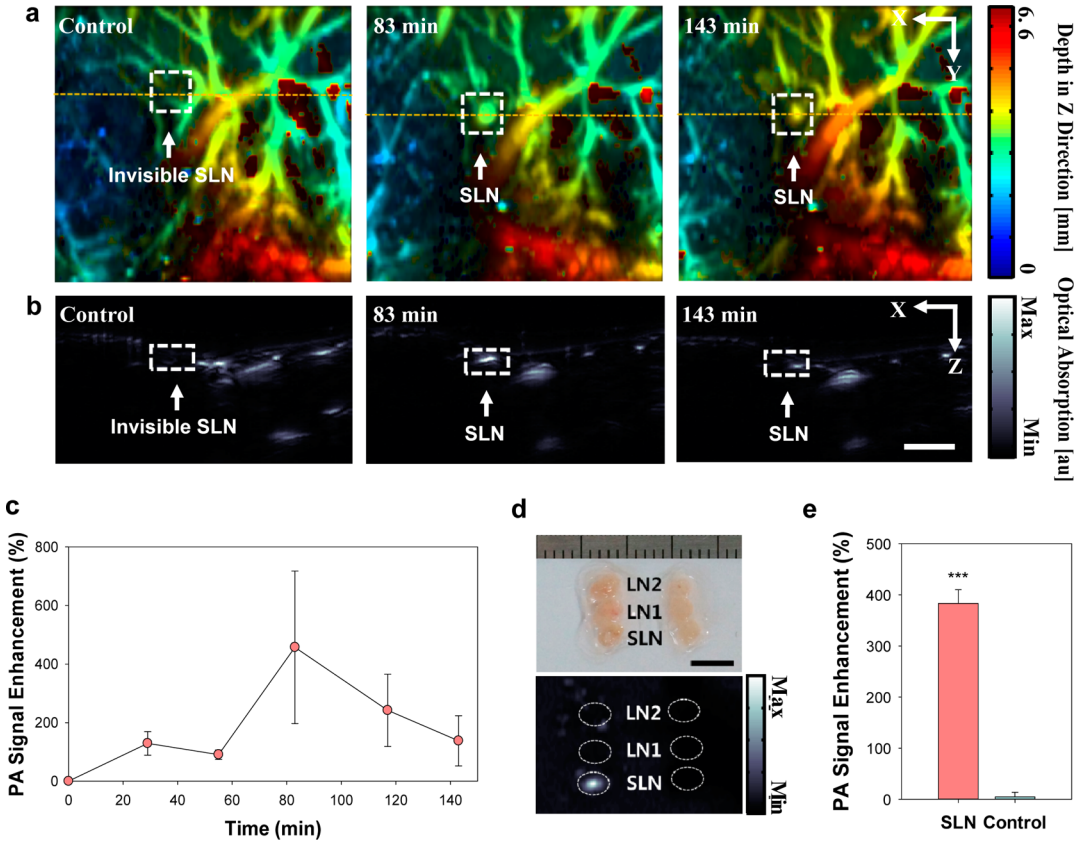


**Figure 4. Photoacoustic tomography of sentinel lymph nodes using GG−melanoidin. (a) Depth-encoded photoacoustic (PA) maximum amplitude projection (MAP) images and (b) cross-sectional PA B-scan images of sentinel lymph nodes (SLNs) before and after intradermal injection of GG−melanoidin (scale bar = 5 mm). (c) PA signal quantification showing the accumulation and elimination of GG−melanoidin in a SLN with increasing time ($n$ = 3). (d) *Ex vivo* photograph and PA MAP image of excised SLNs and adjacent lymph nodes (LNs) after injection of GG−melanoidin (left column) and the control (right column) (scale bar = 5 mm). (e) PA signal quantification of excised SLNs (***$P$ < 0.001).**

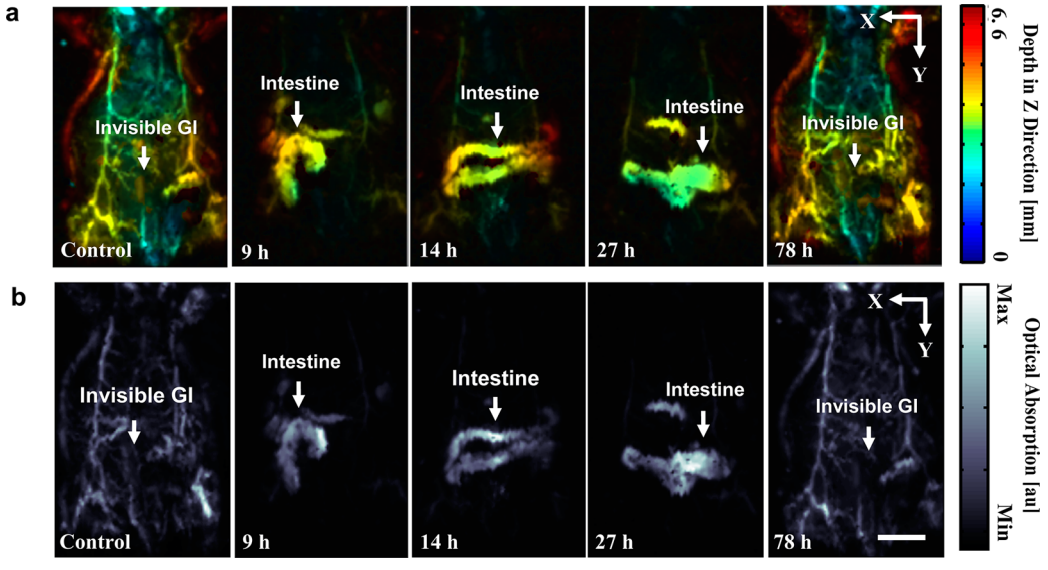


**Figure 5. Photoacoustic tomography of GI tract using GG−melanoidin. (a) Depth-encoded PA maximum amplitude projection (MAP) images and (b) PA MAP images visualizing gastrointestinal (GI) tract with increasing time after oral administration of GG−melanoidin (scale bar = 10 mm).**

decreased to 137.9 ± 85.8% at 143 min (Figure 4c, $n$ = 3). The results revealed that melanoidin initially accumulated and then eliminated or degraded in the SLN after circulating in the lymphatic system. To validate the *in vivo* PA imaging results, we excised draining lymph nodes and control lymph nodes from the axillary region of rats for *ex vivo* PA imaging (Figure 4d).



DOI: 10.1021/acsnano.5b05931
*ACS Nano* 2016, 10, 822−831

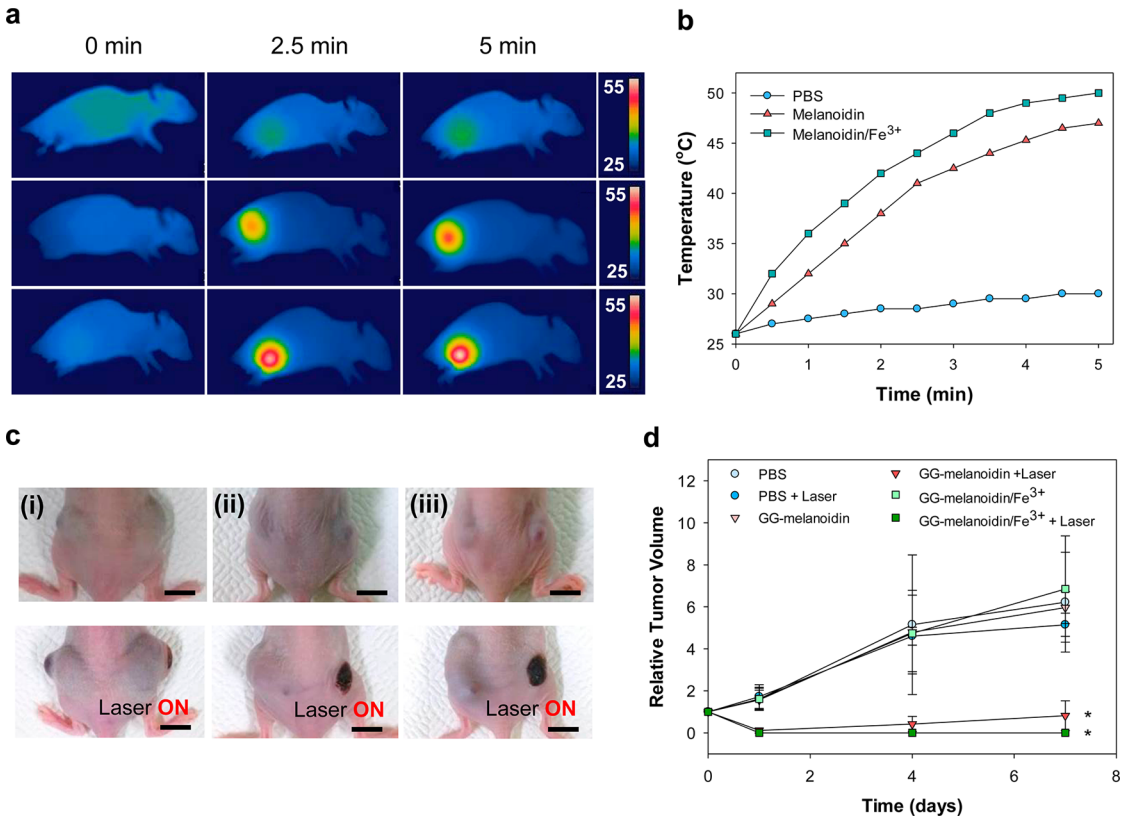


**Figure 6. Photothermal cancer therapy using GG−melanoidin. (a) Infrared camera images showing the change in temperature after subcutaneous injection of (top) PBS, (middle) GG−melanoidin, and (bottom) GG−melanoidin/$Fe^{3+}$ complex into mice with laser irradiation at 808 nm. (b) Temperature change in three aqueous solutions of PBS, GG−melanoidin, and GG−melanoidin/$Fe^{3+}$ complex with laser irradiation at 808 nm. (c) Photographs showing the photothermal ablation cancer therapy using (i) PBS, (ii) GG−melanoidin, and (iii) GG−melanoidin/$Fe^{3+}$ complex with laser irradiation at 808 nm (scale bar = 1 cm). (d) Relative tumor volumes ($V/V_0$) for up to 7 days after photothermal therapy (*$P$ < 0.05 for GG−melanoidin and GG−melanoidin/$Fe^{3+}$ complex *versus* PBS).**

Interestingly, only SLNs could be photoacoustically visualized *ex vivo* with a PA contrast of 383.2 ± 26.7% (Figure 4e), whereas all other successive lymph nodes were not visualized possibly due to the biodegradation or clearance of GG−melanoidin. The selective visualization of SLNs is significantly meaningful to minimize false positives in clinical axillary staging of cancer.

**Photoacoustic Imaging of GI Tract.** We further investigated the orally delivered GG−melanoidin for PA imaging of GI tract. The standard X-ray imaging or computed tomography (CT) plays a leading role in this purpose using iodine or barium swallowed as a contrast agent.[3] However, ionizing radiation applied to the body is energetic enough to directly or indirectly damage DNA. In addition, the contrast agents can possibly cause minor negative side effects such as nausea and vomiting, and severe ones such as anaphylaxis, hypotensive shock, and renal dysfunction.[27] Although micelles using hydrophobic naphthalocyanine dyes were investigated for PA imaging of GI tract,[3] GG−melanoidin might be a perfect candidate for oral administration, because it is one of the components in various foods and expected to be completely excreted in feces. Balb/c nu/nu mice were starved and imaged before and after oral administration of GG−melanoidin. After administration, the passage of GG−melanoidin through the invisible GI tract was clearly visualized over time (Figure 5). Duodenum, intestinal features, and colon were detected distinguishably. After all GG−melanoidin had been digested or excreted (*i.e.*, 78 h later), the GI tract was again invisible.

**Photothermal Cancer Therapy.** Before the applications to PTT, *in vivo* photothermal effect of GG−melanoidin and GG−melanoidin/$Fe^{3+}$ complex was monitored with an infrared camera after subcutaneous injection (0.1 mL, 20 mg/mL) into Balb/c nu/nu mice followed by irradiation of an NIR laser (808 nm, 2 W/$cm^2$) (Figure 6a). The light-to-heat conversion efficiencies were assessed by monitoring the solution temperature during irradiation of the NIR laser for 5 min (Figure 6b). At a concentration of 20 mg/mL, the temperature of GG−melanoidin/$Fe^{3+}$ complex solution reached 50 °C more rapidly than did GG−melanoidin solution due to the enhanced NIR absorption. This temperature was considered to be high enough for photothermal ablation of cancer cells. We assessed the antitumor effect of PTT in B16F10 melanoma-bearing mice (Figure 6c). After intratumoral injection of PBS, GG−melanoidin, or GG−melanoidin/$Fe^{3+}$ complex followed by NIR laser irradiation for 10 min, the tumor volume of mice was monitored for 7 days. The injection of GG−melanoidin or GG−melanoidin/$Fe^{3+}$ complex with laser irradiation resulted in complete ablation of tumors. Especially, after the injection of GG−melanoidin/$Fe^{3+}$ complex and subsequent laser irradiation, tumors did not regrow at least for 7 days. The GG−melanoidin/$Fe^{3+}$ complex increased in size might be more effective for photothermal ablation cancer therapy. In contrast, the tumors grew rapidly in control groups treated with PBS, laser irradiation, GG−melanoidin, or GG−melanoidin/$Fe^{3+}$ complex without laser irradiation (Figure 6d).



DOI: 10.1021/acsnano.5b05931
*ACS Nano* 2016, 10, 822−831

**Photothermal Lipolysis.** The GG−melanoidin was further applied to photothermal lipolysis for obesity therapy or plastic surgery. To show the feasibility of PA imaging for fatty tissues, we photoacoustically imaged a piece of pork belly containing fatty tissues and muscles (Figure S10). Two optical wavelengths were selected, 1210 nm where lipids absorb light dominantly and 1300 nm as a control.[28] The fatty region was clearly visualized on the PA image at 1210 nm, whereas no significant difference was observed between the fatty region and muscles at 1300 nm. After that, *in vivo* adipose tissue ablation of GG−melanoidin was carried out in C56bl/6 mice fed with a high-fat diet for 10 weeks. *In vivo* noninvasive PA MAP image at 1210 nm clearly showed the distribution of subcutaneous fat in the belly region (Figure 7a-i). After subcutaneous injection

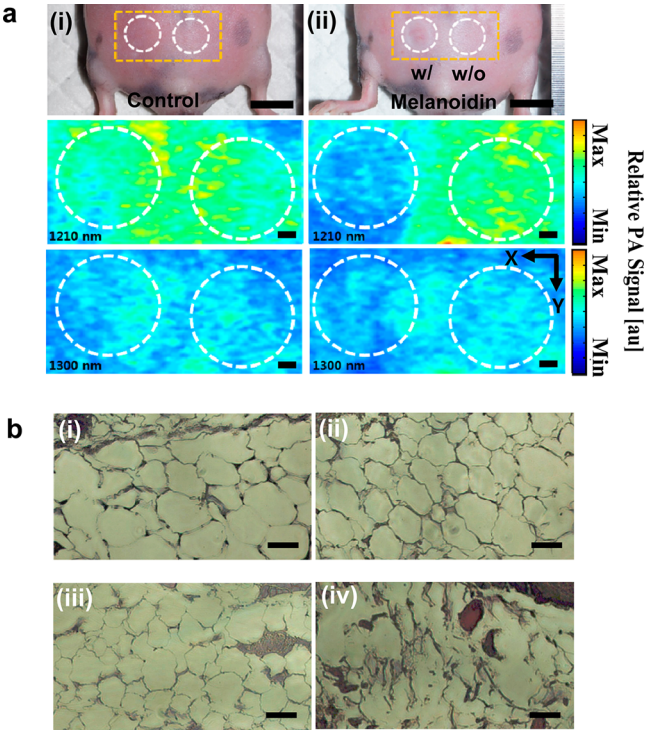


**Figure 7. Photothermal lipolysis using GG−melanoidin.** (a) **Photographs (scale bar = 1 cm) and photoacoustic images (scale bar = 1 mm) at (top) 1210 nm and (bottom) 1300 nm for the lipolysis of subcutaneous fat (i) before and (ii) after photothermal treatment with and without subcutaneous injection of melanoidin.** (b) **Histological analysis of adipose tissues treated by the injection of (i) the control and (ii) GG−melanoidin without laser irradiation, and (iii) the control and (iv) GG−melanoidin with laser irradiation (scale bar = 25 μm).**

of melanoidin, *in vivo* PA imaging revealed that NIR laser irradiation at 808 nm for 10 min induced significant lipolysis of subcutaneous fat, whereas laser irradiation without GG−melanoidin caused no significant change (Figure 7a-ii). *In vivo* PA images at 1,300 nm showed no difference before and after treatment. Histological analysis of the treated tissues with H&E staining confirmed the effective adipose tissue destruction induced by the transmembrane lipolysis and necrosis of adipose cells[29] after GG−melanoidin injection and the following laser irradiation (Figure 7b).

**Clearance of GG−Melanoidin.** Finally, we investigated the body distribution and clearance of GG−melanoidin *via* PA imaging after its subcutaneous injection. The control PA image visualized the blood vessels close to the skin surface, but did not show the bladder. At 38 min post-injection of GG−melanoidin, the bladder appeared with an enhanced PA signal. As time elapsed, GG−melanoidin disappeared from the injection site, but accumulated in the bladder (Figures 8a and S11a). We also obtained depth-resolvable cross-sectional PA images (Figure 8b). The PA signal amplitude at the bladder gradually increased up to 214 min post-injection and then saturated ($n$ = 3, Figure S11b). It was remarkable that GG−melanoidin could be used to effectively visualize the urinary tract for leaks or fistulas. The results clearly showed that GG−melanoidin was removed from the body by renal clearance after subcutaneous injection.

We also quantified the urinary excretion to assess the renal clearance of GG−melanoidin and GG−melanoidin/$Fe^{3+}$ complex in comparison to MB (Figure 8c). The amount of urinary excretion after 4 days was *ca.* 76% for 5 kDa GG−melanoidin, *ca.* 65% for 10 kDa GG−melanoidin, and *ca.* 52% for GG−melanoidin/$Fe^{3+}$ complex. Although GG−melanoidin was not completely removed in 4 days, the remaining melanoidin might degrade over time in the body. As shown in Figures 8d and S11c, GG−melanoidin degraded significantly in the presence of hydrogen peroxide (HP), whereas it remained stable in 50% serum enabling the applications to PAT and PTT. HP exists in phagocytes and many organs, and induces oxidative stress response and necrotic cell death at high levels.[30] Melanoidin is reported to show an antioxidative effect on HP.[22,23] In contrast, despite the small size, only *ca.* 28% of MB was excreted after 4 days, possibly due to the cellular uptake or adhesion to organs. We observed significant hair loss and necrosis at the injection site of MB, compared to no sign of abnormality for the cases of GG−melanoidin and GG−melanoidin/$Fe^{3+}$ complex (Figure S12). The long-term cytocompatibility of GG−melanoidin and GG−melanoidin/$Fe^{3+}$ complex was also clearly confirmed by the blood biochemistry assay (Figure S13) and histological analysis with H&E staining one month post-injection (Figure S14).

## CONCLUSIONS

We successfully demonstrated the feasibility of optically active biodegradable polymer of GG−melanoidin for PA imaging of sentinel lymph nodes and GI tract, and for photothermal cancer therapy and lipolysis. GG−melanoidin was easily synthesized by nonenzymatic Maillard reaction and showed strong optical absorbance in the NIR region. GG−melanoidin was size-controllable, cytocompatible, biodegradable, and excretable by renal clearance. These are the unique characteristics of polymeric melanoidin in contrast to other nanomaterials for PAT and PTT. Especially, melanoidin, synthesized using carbohydrates and amino acids, can be one of the best contrast agents for GI tract imaging as a component of foods. Furthermore, the versatile complex formation with metal ions like $Fe^{3+}$ and functionalization with target moieties enable a variety of applications to theranostic nanomedicines.

## MATERIALS AND METHODS

**Materials.** Glucose, glycine, iron(III) chloride hexahydrate, sodium bicarbonate, albumin from chicken egg white, gold chloride trihydrate, hexadecyltrimethylammonium bromide, methylene blue, sodium borohydride, and silver nitrate were obtained from Sigma-Aldrich (St. Louis, MO). Dulbecco's Modified Eagle's Medium (DMEM), fetal bovine serum (FBS), antibiotics, and phosphate buffered saline (PBS) tablet were purchased from Invitrogen Co. (Carlsbad, CA). MTT


DOI: 10.1021/acsnano.5b05931
*ACS Nano* 2016, 10, 822−831

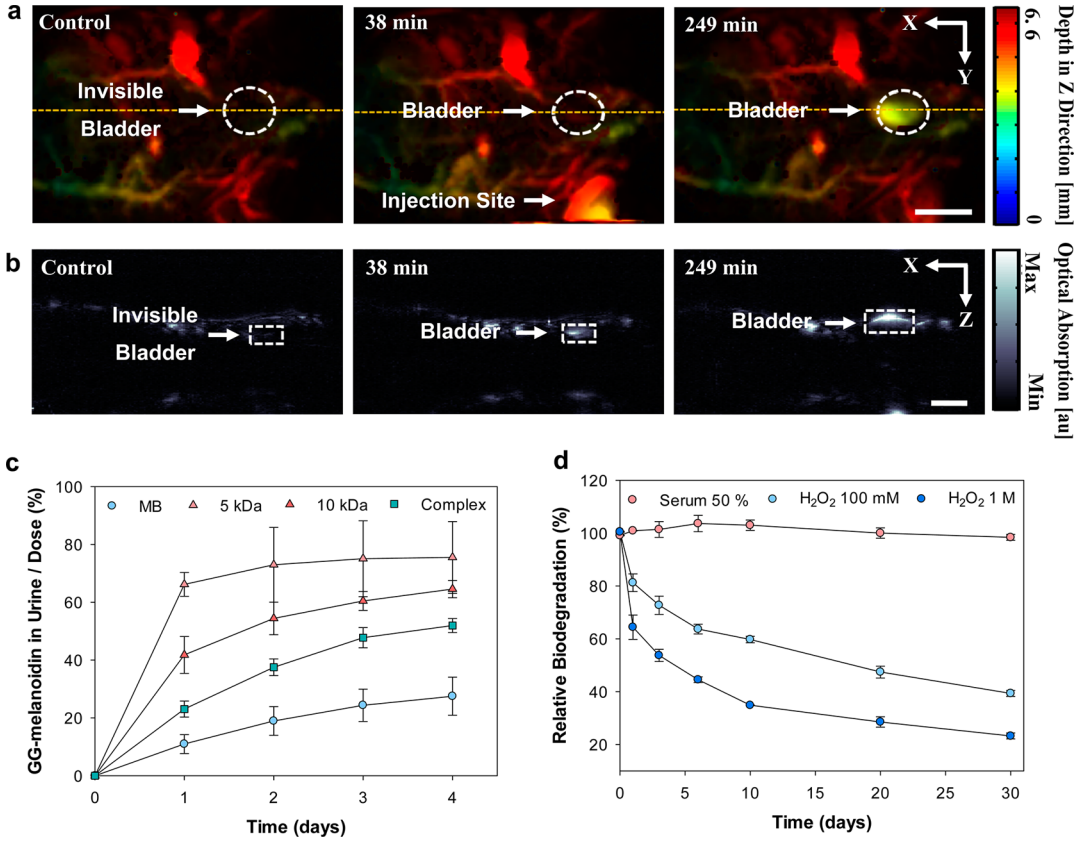


**Figure 8. Renal clearance and biodegradation of GG−melanoidin. (a) Whole body depth-encoded PA MAP images and (b) cross-sectional PA B-scan images after subcutaneous injection of GG−melanoidin (scale bar = 10 mm). (c) The urinary excretion of methylene blue (MB), GG−melanoidin with a molecular weight of 5 and 10 kDa, and that from GG−melanoidin/$Fe^{3+}$ complex after subcutaneous injection. (d) Relative biodegradation (%) of GG−melanoidin in 50% serum, 100 mM of $H_2O_2$, and 1 M of $H_2O_2$ determined by measuring the absorbance at 450 nm with increasing time.**

assay kit was obtained from Promega Co. (Madison, WI). B16F10 and FL83B cells line were purchased from ATCC (Manassas, VA).

**Synthesis of GG−Melanoidin.** GG−melanoidin was synthesized using 1 g of glucose and 2 g of glycine dissolved in 10 mL of DI water. The solution pH was adjusted to 7.4 using 1 M solution of NaOH (or sodium bicarbonate). For comparison, 1 g of glucose was dissolved in 10 mL of DI water, which was adjusted to pH 7.4. The solutions were incubated with stirring at 37 °C for 2 weeks. The MW of GG−melanoidin was controlled by changing the incubation time. The resulting product was purified by dialysis against a large excess amount of DI water for 3 days and lyophilized for 3 days. The pH of GG−melanoidin solution was adjusted to 7.4 using a NaOH solution before *in vitro* and *in vivo* experiments.

**Formation of GG−Melanoidin/$Fe^{3+}$ Complex.** The GG−melanoidin/$Fe^{3+}$ complex was prepared by adding GG−melanoidin solution (MW = 10 kDa, 0.5 mL of 40 mg/mL) to $FeCl_3{\cdot}6H_2O$ solution (0.5 mL of 20 mg/mL) and incubating the mixed solution with stirring for 1 h. The resulting product was purified by dialysis against a large excess amount of DI water for 3 days and lyophilized for 3 days. The pH of GG−melanoidin/$Fe^{3+}$ complex solution was adjusted to 7.4 using a NaOH solution before *in vitro* and *in vivo* experiments.

**Cytotoxicity Test.** For the assessment of cytotoxicity, $2 \times 10^4$ cells of FL83B liver cell line and B16F10 cancer cell line were seeded and incubated for 24 h in a 96-well plate containing DMEM with 10% FBS. Then, the cells were treated with GG−melanoidin, GG−melanoidin/$Fe^{3+}$ complex, GCD, or MB at the specified concentrations. Before the treatments, the solution pH of GG−melanoidin and GG−melanoidin/$Fe^{3+}$ complex was adjusted to that of the medium. After 12 h, the media were replaced with fresh media and then MTT was added to the solution. After 2 h, the media were replaced with dimethyl sulfoxide to determine the cell viability by measuring the absorbance at 540 nm ($n$ = 3).

***In Vitro*, *in Vivo*, and *ex Vivo* PA Imaging.** To measure the PA sensitivity of GG−melanoidin spectrum *in vitro*, we imaged four silicon tubes filled with DI water or aqueous solutions of GG−melanoidin with a MW of 5, 7, and 10 kDa at a concentration of 20 mg/mL by varying PA excitation wavelengths from 680 to 900 nm. To further compare the PA signals of various agents, we photoacoustically imaged five silicon tubes filled with DI water or solutions of GG−melanoidin, GG−melanoidin/$Fe^{3+}$ complex, AuNR, and MB at the same mass concentration of 20 mg/mL or at the same optical density of 1.3 $mm^{-1}$ at an optical wavelength of 680 nm. All *in vivo* animal experiments complied with the guidelines of the Pohang University of Science and Technology (POSTECH) on the care and use of laboratory animals.

For *in vivo* sentinel lymph node PA imaging, we first anesthetized female Sprague−Dawley (SD) rats weighing *ca.* 250 g with a mixture of ketamine (85 mg/kg) and xylazine (15 mg/kg), and then the anesthesia was maintained using a vaporized-isoflurane system. We photoacoustically visualized the axillary vasculature networks and lymphatic systems of the rats before and after intradermal injection of GG−melanoidin (0.1 mL, 20 mg/mL) ($n$ = 3). After *in vivo* PA imaging, we excised the lymph nodes to perform *ex vivo* PA imaging for validation. For *in vivo* PA imaging of GI track, female Balb/c nu/nu mice weighing *ca.* 20 g were first starved and used for PA imaging as the control. After oral delivery of GG−melanoidin (0.3 mL, 20 mg/mL) by gavage, the abdominal region was photoacoustically imaged. *Ex vivo* PA image of pork belly was acquired at 1210 nm for lipid using that at 1300 nm as a control. *In vivo* PA imaging of adipose tissue was carried out in C56bl/6 mice weighing *ca.* 50 g fed with high-fat diet for 10 weeks. After acquiring PA images of the abdomen at 1210 and 1300 nm, the GG−melanoidin (0.1 mL, 20 mg/mL) was injected into the



DOI: 10.1021/acsnano.5b05931
*ACS Nano* 2016, 10, 822−831

subcutaneous fat with 808 nm laser irradiation (2 W/cm$^2$) for 10 min. After photothermal lipolysis, the PA images were obtained again at 1210 and 1300 nm. For *in vivo* PA imaging of bladder, female Balb/c nu/nu mice were fully anesthetized as described above. After acquiring the whole-body control PA images of the abdomen, GG−melanoidin (0.1 mL, 20 mg/mL) was injected subcutaneously into the left leg. Renal clearance was photoacoustically monitored for 280 min post-injection ($n$ = 3).

**Photothermal Cancer Therapy.** For temperature monitoring *in vivo*, female Balb/c nu/nu mice were anesthetized by intraperitoneal injection of a combination of ketamine (100 mg/kg) and xylazine (10 mg/kg), and then treated by subcutaneous injection of PBS, GG−melanoidin, or GG−melanoidin/$Fe^{3+}$ complex (0.1 mL, 20 mg/mL) through a 26-gauge needle into the right flank. During 808 nm laser irradiation (2 W/cm$^2$), the body temperature of mice was recorded using an infrared camera (Mikroshot). For photothermal therapy of tumor model mice, B16F10 tumor cells ($2 \times 10^6$ cells) were injected into each right and left flank of female Balb/c nu/nu mice (age of 5 weeks, weight of *ca.* 20 g). When tumor volumes reached *ca.* 200 mm$^3$, the mice were anesthetized by intraperitoneal injection of a combination of ketamine (100 mg/kg) and xylazine (10 mg/kg). Then, the right and left tumors were treated by a single intratumoral injection of the sample of PBS, GG−melanoidin, or GG−melanoidin/$Fe^{3+}$ complex (0.1 mL, 20 mg/mL) through a 26-gauge needle. Then, only right tumors were irradiated with an 808 nm laser (2 W/cm$^2$) for 10 min. All mice were housed under a standard condition of a 12 h light/dark cycle with free access to food and water, and tumor volumes were measured for a week post-treatment ($n$ = 3).

**Photothermal Lipolysis.** C56bl/6 mice fed with a high-fat diet for 10 weeks were fully anesthetized by intraperitoneal injection of a combination of ketamine (100 mg/kg) and xylazine (10 mg/kg). After that, the abdomens were treated by a single subcutaneous injection of GG−melanoidin (0.1 mL, 20 mg/mL) through a 26-gauge needle. Then, injection sites were irradiated with an 808 nm laser (2 W/cm$^2$) for 10 min. Four adipose tissue sites for the control, GG−melanoidin injection, laser irradiation, and GG−melanoidin injection with laser irradiation were collected and analyzed with H&E staining.

**Renal Clearance.** GG−melanoidin with a MW of 5 or 10 kDa, GG−melanoidin/$Fe^{3+}$ complex, or methylene blue (MB) was subcutaneously injected to 5-week-old female Balb/c mice (0.1 mL, 20 mg/mL) through a 26-gauge needle. The mice were transferred to metabolic cages. The urine was separately collected daily for 5 days and kept at −20 °C until analysis. To determine the recovery percentages, the absorbance of urine was measured at 450 nm for GG−melanoidin and GG−melanoidin/$Fe^{3+}$ complex, and at 650 nm for MB ($n$ = 3).

**Biodegradation Test.** For biodegradation tests, 1 mL of GG−melanoidin (2 mg/mL in PBS, pH 7.4) was added to 1 mL of serum or $H_2O_2$ solution (200 mM or 2 M). After incubation at 37 °C with shaking for a specified time, 50 μL of the samples was collected and kept at −20 °C. The absorption was measured at 450 nm for 30 days ($n$ = 3).

## ASSOCIATED CONTENT

### Supporting Information

The Supporting Information is available free of charge on the ACS Publications website at DOI: 10.1021/acsnano.5b05931.

Experimental details and additional figures (PDF)

## AUTHOR INFORMATION


### Corresponding Authors

*E-mail: chulhong@postech.ac.kr.

*E-mail: skhanb@postech.ac.kr.

### Present Address

[‖](M.J.) School of Electronics Engineering, Kyungpook National University (KNU), 80 Daehak-ro, Daegu 702-701, Korea

### Author Contributions

[§]M.-Y.L., C.L., and H.S.J. contributed equally to this work.


### Notes

The authors declare no competing financial interest.

## ACKNOWLEDGMENTS

This research was supported by the MSIP (Ministry of Science, ICT and Future Planning), Korea, under the "ICT Consilience Creative Program" (IITP-2015-R0346-15-1007) supervised by the IITP (Institute for Information & Communications Technology Promotion). This research was supported by the Bio & Medical Technology Development Program (No. 2012M3A9C6049791) and Engineering Research Center Grant (NRF-2011-0030075) of the National Research Foundation (NRF). This research was supported by a grant of the Korean Health Technology R&D Project, Ministry of Health and Welfare, Korea (HI14C1658).

## REFERENCES


(1) Wang, L. V.; Hu, S. Photoacoustic Tomography: *In vivo* Imaging from Organelles to Organs. *Science* **2012**, *335*, 1458−1462.

(2) Lovell, J. F.; Jin, C. S.; Huynh, E.; Jin, H.; Kim, C.; Rubinstein, J. L.; Chan, W. C.; Cao, W.; Wang, L. V.; Zheng, G. Porphysome Nanovesicles Generated by Porphyrin Bilayers for Use as Multimodal Biophotonic Contrast Agents. *Nat. Mater.* **2011**, *10*, 324−332.

(3) Zhang, Y.; Jeon, M.; Rich, L. J.; Hong, H.; Geng, J.; Zhang, Y.; Shi, S.; Barnhart, T. E.; Alexandridis, P.; Huizinga, J. D.; et al. Non-Invasive Multimodal Functional Imaging of the Intestine with Frozen Micellar Naphthalocyanines. *Nat. Nanotechnol.* **2014**, *9*, 631−638.

(4) Chen, J. Y.; Yang, M. X.; Zhang, Q. A.; Cho, E. C.; Cobley, C. M.; Kim, C.; Glaus, C.; Wang, L. V.; Welch, M. J.; Xia, Y. N. Gold Nanocages: A Novel Class of Multifunctional Nanomaterials for Theranostic Applications. *Adv. Funct. Mater.* **2010**, *20*, 3684−3694.

(5) Homan, K. A.; Souza, M.; Truby, R.; Luke, G. P.; Green, C.; Vreeland, E.; Emelianov, S. Silver Nanoplate Contrast Agents for *in vivo* Molecular Photoacoustic Imaging. *ACS Nano* **2012**, *6*, 641−650.

(6) Liu, X.; Lee, C.; Law, W. C.; Zhu, D.; Liu, M.; Jeon, M.; Kim, J.; Prasad, P. N.; Kim, C.; Swihart, M. T. Au-Cu(2-x)Se Heterodimer Nanoparticles with Broad Localized Surface Plasmon Resonance as Contrast Agents for Deep Tissue Imaging. *Nano Lett.* **2013**, *13*, 4333−4339.

(7) Huang, P.; Lin, J.; Li, W.; Rong, P.; Wang, Z.; Wang, S.; Wang, X.; Sun, X.; Aronova, M.; Niu, G.; et al. Biodegradable Gold Nanovesicles with an Ultrastrong Plasmonic Coupling Effect for Photoacoustic Imaging and Photothermal Therapy. *Angew. Chem., Int. Ed.* **2013**, *52*, 13958−13964.

(8) De La Zerda, A.; Zavaleta, C.; Keren, S.; Vaithilingam, S.; Bodapati, S.; Liu, Z.; Levi, J.; Smith, B. R.; Ma, T. J.; Oralkan, O.; et al. Carbon Nanotubes As Photoacoustic Molecular Imaging Agents in Living Mice. *Nat. Nanotechnol.* **2008**, *3*, 557−562.

(9) Zha, Z.; Deng, Z.; Li, Z. Y.; Li, C.; Wang, J.; Wang, S.; Qu, E.; Dai, Z. Biocompatible Polypyrrole Nanoparticles as a Novel Organic Photoacoustic Contrast Agent for Deep Tissue Imaging. *Nanoscale* **2013**, *5*, 4462−4467.

(10) Wu, L.; Cai, X.; Nelson, K.; Xing, W.; Xia, J.; Zhang, R.; Stacy, A. J.; Luderer, M.; Lanza, G. M.; Wang, L. V.; et al. A Green Synthesis of Carbon Nanoparticle from Honey for Real-Time Photoacoustic Imaging. *Nano Res.* **2013**, *6*, 312−325.

(11) Pu, K.; Shuhendler, A. J.; Jokerst, J. V.; Mei, J.; Gambhir, S. S.; Bao, Z.; Rao, J. Semiconducting Polymer Nanoparticles as Photoacoustic Molecular Imaging Probes in Living Mice. *Nat. Nanotechnol.* **2014**, *9*, 233−239.

(12) Zu, X.; Yan, R.; Robbins, S.; Krishack, P. A.; Liao, D. F.; Cao, D. Reduced 293T Cell Susceptibility to Acrolein Due to Aldose Reductase-like-1 Protein Expression. *Toxicol. Sci.* **2007**, *97*, 562−568.

(13) Liu, C.; Zhang, P.; Tian, F.; Li, W.; Li, F.; Liu, W. One-Step Synthesis of Surface Passivated Carbon Nanodots by Microwave




DOI: 10.1021/acsnano.5b05931
*ACS Nano* 2016, 10, 822−831

Assisted Pyrolysis for Enhanced Multicolor Photoluminescence and Bioiming. *J. Mater. Chem.* **2011**, *21*, 13163−13167.
(14) Bhunia, S. K.; Saha, A.; Maity, A. R.; Ray, S. C.; Jana, N. R. Carbon Nanoparticle-Based Fluorescent Bioimaging Probes. *Sci. Rep.* **2013**, *3*, 1473.
(15) Erixon, M.; Lindén, T.; Kjellstrand, P.; Carlsson, O.; Ernebrant, M.; Forsbäck, G.; Wieslander, A.; Jönsson, J. A. PD Fluids Contain High Concentrations of Cytotoxic GDPs Directly after Sterilization. *Peritoneal Dial. Int.* **2004**, *24*, 392−398.
(16) Monien, B. H.; Frank, H.; Seidel, A.; Glatt, H. Conversion of the Common Food Constituent 5-Hydroxymethylfurfural into a Mutagenic and Carcinogenic Sulfuric Acid Ester in the Mouse *in vivo*. *Chem. Res. Toxicol.* **2009**, *22*, 1123−1128.
(17) Morgan, L. W.; Wieslander, A.; Davies, M.; Horiuchi, T.; Ohta, Y.; Beavis, M. J.; Craig, K. J.; Williams, J. D.; Topley, N. Glucose Degrataion Products (GDP) Retard Remesothelialization Independently of D-Glucose Concentration. *Kidney Int.* **2003**, *64*, 1854−1866.
(18) Zhang, M.; Yang, H.; Liu, Y.; Sun, X.; Zhang, D.; Xue, D. First Identification of Primary Nanoparticles in the Aggregation of HMF. *Nanoscale Res. Lett.* **2012**, *7*, 38.
(19) Lewinski, N.; Colvin, V.; Drezek, R. Cytotoxicity of Nanoparticles. *Small* **2008**, *4*, 26−49.
(20) Nel, A.; Xia, T.; Mädler, L.; Li, N. Toxic Potential of Materials at the Nanolevel. *Science* **2006**, *311*, 622−627.
(21) Liu, J. H.; Yang, S. T.; Wang, H.; Chang, Y.; Cao, A.; Liu, Y. Effect of Size and Dose on the Biodistribution of Graphene Oxide in Mice. *Nanomedicine* **2012**, *7*, 1801−1812.
(22) Wang, H.; Qian, H.; Yao, W. Melanoidins Produced by the Maillard Reaction: Structure and Biological Activity. *Food Chem.* **2011**, *128*, 573−584.
(23) Cossu, A.; Posadino, A. M.; Giordo, R.; Emanueli, C.; Sanguinetti, A. M.; Piscopo, A.; Poiana, M.; Capobianco, G.; Piga, A.; Pintus, G. Apricot Melanoidins Prevent Oxidative Endothelial Cell Death by Counteracting Mitochondrial Oxidation and Membrane Depolarization. *PLoS One* **2012**, *7*, e48817.
(24) Tessier, F. J. The Maillard Reaction in the Human Body. The Main Discoveries and Factors That Affect Glycation. *Pathol. Biol.* **2010**, *58*, 214−219.
(25) Kroh, L. W.; Fiedler, T.; Wagner, J. $\alpha$-Dicarbonyl Compounds-Key Intermediates for the Formation of Carbohydrate-Based Melanoidins. *Ann. N. Y. Acad. Sci.* **2008**, *1126*, 210−215.
(26) Hayase, F.; Usui, T.; Ono, Y.; Shirahashi, Y.; Machida, T.; Ito, T.; Nishitani, N.; Shimohira, K.; Watanabe, H. Formation Mechanisms of Melanoidins and Fluorescent Pyridinium Compounds as Advanced Glycation End Products. *Ann. N. Y. Acad. Sci.* **2008**, *1126*, 53−58.
(27) Maddox, T. G. Adverse Reactions to Contrast Material: Recognition, Rrevention, and Treatment. *Am. Fam. Physician* **2002**, *66*, 1229−1235.
(28) Allen, T. J.; Hall, A.; Dhillon, A. P.; Owen, J. S.; Beard, P. C. Spectroscopic Photoacoustic Imaging of Lipid-Rich Plaques in the Human Aorta in the 740 to 1400 nm Wavelength Range. *J. Biomed. Opt.* **2012**, *17*, 061209.
(29) Yanina, I. Y.; Tuchin, V. V.; Navolokin, N. A.; Matveeva, O. V.; Bucharskaya, A. B.; Maslyakova, G. N.; Altshuler, G. B. Fat Tissue Histological Study at Indocyanine Green-Mediated Photothermal/Photodynamic Treatment of the Skin *in vivo*. *J. Biomed. Opt.* **2012**, *17*, 058002.
(30) Rhee, S. G. Cell signaling. $H_2O_2$, a Necessary Evil for Cell Signaling. *Science* **2006**, *312*, 1882−1883.



DOI: 10.1021/acsnano.5b05931
*ACS Nano* 2016, 10, 822−831